

PAPER

## Spiral phase plasma mirror

To cite this article: Elkana Porat *et al* 2022 *J. Opt.* **24** 085501

View the [article online](#) for updates and enhancements.

### You may also like

- [On-shot characterization of single plasma mirror temporal contrast improvement](#)  
L Obst, J Metzkes-Ng, S Bock *et al.*
- [Optimization of plasma mirror reflectivity and optical quality using double laser pulses](#)  
G G Scott, V Bagnoud, C Brabetz *et al.*
- [Quantum vacuum processes in the extremely intense light of relativistic plasma mirror sources](#)  
Antonin Sainte-Marie, Luca Fedeli, Neïl Zaïm *et al.*



**IOP | ebooks™**

Bringing together innovative digital publishing with leading authors from the global scientific community.

Start exploring the collection—download the first chapter of every title for free.

# Spiral phase plasma mirror

Elkana Porat<sup>1,2,3,\*</sup> , Shlomi Lightman<sup>3</sup>, Itamar Cohen<sup>1,2</sup> and Ishay Pomerantz<sup>1,2</sup> 

<sup>1</sup> The School of Physics and Astronomy, Tel Aviv University, Tel Aviv 69978, Israel

<sup>2</sup> Center for Light–Matter Interaction, Tel Aviv University, Tel Aviv 69978, Israel

<sup>3</sup> Applied Physics Division, Soreq NRC, Yavne, 81800, Israel

E-mail: [elkanaporat@mail.tau.ac.il](mailto:elkanaporat@mail.tau.ac.il)

Received 13 March 2022, revised 6 June 2022

Accepted for publication 17 June 2022

Published 5 July 2022



CrossMark

## Abstract

In this work we present a method for generating ultra-intense Laguerre–Gauss laser beams, using 3D direct laser writing of spiral phase plasma mirrors. These single-use mirrors provide an economical and scalable solution for arbitrary spatial beam shaping at ultra-high laser intensities. The use of these plasma-based optical devices is demonstrated for the case of an orbital angular momentum of  $l = 1$ , with incident laser intensity of  $10^{17} \text{ W cm}^{-2}$ . We conclude by discussing practical considerations for using these optical elements on petawatt-class laser systems

Keywords: plasma mirror, laser-plasma interaction, beam shaping, orbital angular momentum, direct laser writing

(Some figures may appear in colour only in the online journal)

## 1. Introduction

Laguerre–Gaussian (LG) light beams can have a rotating azimuthal phase,  $\exp[-i(\omega t - kz) - il\phi]$ , which carries a quantized orbital angular momentum (OAM) of  $\hbar l$  per photon, with  $l$  being a positive or negative integer [1]. In the quarter of a century since its discovery, OAM-carrying beams were applied in various fields, including optical tweezers [2], microscopy [3], optical communication [4] and quantum computing [5].

The introduction of OAM to laser beams in the relativistic limit (above  $10^{18} \text{ W cm}^{-2}$ ) is expected to drive new types of laser-plasma dynamics, such as optical plasma cutters [6] or drills [7], and may offer new means of accelerating electrons [8] or ions [7], and generating attosecond electron pulses [9], vortex harmonics [10, 11], and gamma rays [12].

Experimental realization of OAM beams at relativistic intensities is challenging because of non-linear optical effects and damage to conventional spatial phase modulators. These effects can be mitigated by simply limiting the laser intensity [13], or by placing the phase element early in the laser amplification chain [14], or by the fabrication of large-diameter *reflective* phase elements [15, 16]. Out of these mentioned

solutions, the latter hold the most potential for wide-use applications, as it does not require modifications to the laser system itself. However, state-of-the-art multi-petawatt (PW) laser systems would require 10 s of cm size optical elements, which are still a considerable fabrication challenge.

Plasma-based optical phase modulators, however, are not subject to these limitations. To form a plasma mirror, one must ensure that the plasma expansion prior to the main interaction is negligible with respect to the light wavelength. Having this condition fulfilled, plasma mirrors act much like metallic mirrors, thus retain the original polarization and coherence of the incident laser beam [17]. As one of the simplest plasma-based optical element is the plasma mirror, its use for relativistic OAM beams realization is natural. Indeed, PM-based generation of an OAM beam was demonstrated by Leblanc *et al* [18], who optically induced transient fork-pattern grating modulations to a flat PM. His method, however, suffers from low coupling to the OAM modes because of low diffraction efficiency. Other concepts of acquiring a rotating azimuthal phase during propagation in plasma, such as the plasma  $q$ -plate [19] and plasma parametric amplification [20], are highly challenging to implement and are yet to be realized.

An alternative suggestion by Shi *et al* [21] is to imprint OAM on a high intensity laser beam by reflection off a spiral

\* Author to whom any correspondence should be addressed.

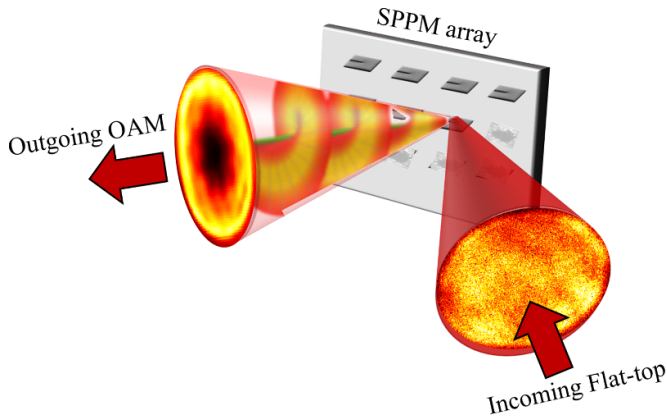


**Figure 1.** Illustration of the SPPM beam shaping method. An intense laser beam irradiates a microscopic 3D printed spiral phase target, which reflect the beam with an added OAM as a SPPM. A new target is positioned in the beam path before the next laser shot.

phase plasma mirror (SPPM). In this paper, we present the first experimental realization of SPPMs, using 3D direct laser writing (3D-DLW) fabrication. As illustrated in figure 1, upon intense irradiation the 3D printed spiral phase targets ionize to become SPPMs, which induce OAM to the reflected laser field. These single-use mirrors provide an economical and scalable solution for arbitrary spatial beam shaping at ultra-high laser intensities.

## 2. Method

The total optical path difference induced by a spiral phase optical element is given by:

$$\delta_{\text{SPP}}(x, y; l) = \frac{\lambda l}{2\pi} \tan^{-1}(y, x), \quad (1)$$

where the  $\tan^{-1}$  function is defined to eliminate the quadrant ambiguity of the arctangent function. In the case of reflective optic, the optical path difference is related to twice the vertical displacement of the reflective surface. The angle of incidence (AOI) imposes two design considerations for a reflective optical element. First, the height must be matched to the  $\cos \theta_{\text{AOI}}$  reduction in the accumulated phase upon reflection. Second, a one-dimensional stretch of  $1/\cos \theta_{\text{AOI}}$  should match for the stretch of the incident beam illuminating the surface in the plane of incidence. With these corrections, the vertical displacement becomes:

$$h_{\text{SPPM}}(x, y; l) = \frac{\lambda l}{4\pi \cos \theta_{\text{AOI}}} \tan^{-1}(y, x \cos \theta_{\text{AOI}}), \quad (2)$$

where  $x$  is oriented along the plane of incidence. Similarly, the lateral dimension of the target along the plane of incidence must be extended by  $1/\cos \theta_{\text{AOI}}$  to ensure that the elongated focal spot is fully contained within the SPPM. Equation (2) gives the vertical displacement along the rotation angle. 3D-DLW fabrication of such continuous spiral phase

plate [22] would require a stage resolution better than 10 nm. Since the SPPMs are destroyed at each laser shot, an economic step-like design is favored to reduce fabrication time and cost. The main disadvantage of a discrete design is a reduction in the efficiency, defined as the amount of energy in the designed LG mode relative to the total energy of the reflected beam. Here, an eight-step discretization was chosen, which is expected to induce up to a 5% efficiency degradation [23]. For higher OAM with  $|l| > 1$ , larger number of steps will be favored. The designed height map of an  $l = 1$  SPPM element for an AOI of  $55^\circ$  is presented in figure 2(a). The eight-steps design results from a 100 nm discretization of equation (2).

Fabrication of the 3D-DLW SPPMs was carried out using a commercial femtosecond laser lithography system (Photonic Professional GT, Nanoscribe GmbH, Germany). We fabricated these optics with lateral dimensions of  $40 \times 60 \mu\text{m}^2$ , roughly twice larger than the focal spot. The designed structures were printed layer by layer on a 2 cm wide square sapphire substrate, with 100 nm layer thickness increments. For adequate adhesion, the SPPM surfaces were printed on a  $4 \mu\text{m}$  pedestal above the substrate. After fabrication the targets were coated with a 50 nm layer of Au to increase their low-intensity reflectivity and to protect the printed structures. The targets were examined with a SEM before and after the final coating, to assure the structured targets were not affected.

A topographic scan and an SEM image of one printed SPPM, are shown in figures 2(b) and (c) respectively. The eight-fold discrete helical surface is clearly seen on the image, as well as the height discontinuity corresponding to a  $2\pi$  phase jump. The image reveals an overall convex curvature overlaid on the helical structure, possibly a result of shrinkage of the photoresist layers during the fabrication process. In mass production of SPPM targets, such a curvature may be nullified by optimizing the photoresist development procedure. For this proof-of-concept campaign, however, we evaluated the spatial phase induced by the fabricated SPPMs using the numeric fit of equation (2) to the height map of figure 2(b). Here, a second-order polynomial surface is added, and  $l$  is taken as a free parameter:

$$z(x, y) = h_{\text{SPPM}}(x, y; l) + \frac{(x - x_0)^2}{2R_x} + \frac{(y - y_0)^2}{2R_y} + \frac{xy}{R_{xy}}. \quad (3)$$

The fitting procedure yields a topological charge value of  $l = 0.95 \pm 0.005$ , with radii of curvature (ROC)  $R_x = -1290 \mu\text{m}$  and  $R_y = -670 \mu\text{m}$ , along the  $x$  and  $y$  axes, respectively. The residual shape error is  $0.128 \mu\text{m}$  (RMS), roughly  $\lambda/6$  for a Ti:Sapphire laser system with  $0.8 \mu\text{m}$  central wavelength. The short-scale surface roughness was measured to be about  $\lambda/13$  (RMS). Although this value is somewhat higher than the roughness of optically polished glass substrates, an order-of-magnitude reduction of the short-scale roughness is expected owing to plasma expansion [24].

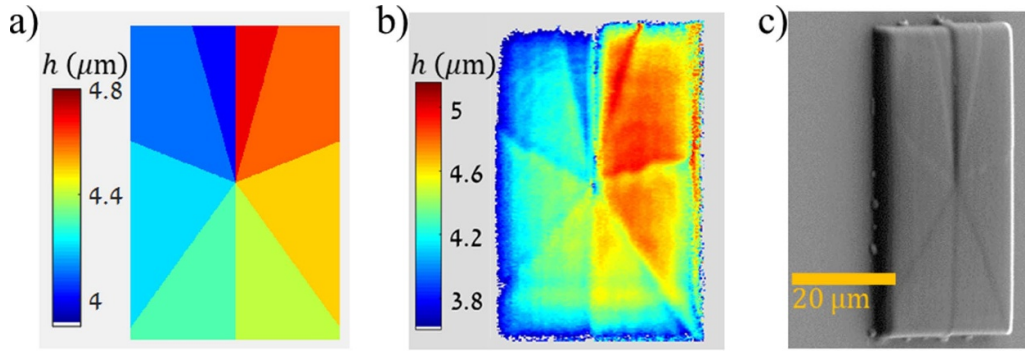


**Figure 2.** (a) Designed height map of the target, given by 100 nm discretization of equation (2). (b) Topographic scan (top view) of the target; color scale is in micrometers. The magnification is similar to the SEM image. (c) SEM image of an SPPM target, designed for  $l = 1$  and  $\theta_{AOI} = 55^\circ$ . Lateral dimensions of the target are  $40 \times 60 \mu\text{m}^2$ .

### 3. Experimental demonstration

We first characterized the OAM imprinted by the SPPMs on a low-power CW laser beam at  $\lambda = 785 \text{ nm}$ . An  $f/20$  lens focused the beam onto an  $l = 1$  SPPM at  $\theta_{AOI} = 55^\circ$ . Near-field (NF) patterns were imaged directly on a CCD positioned a few cm downstream. Figure 3 shows the evolution of the NF pattern as the SPPM position is varied with respect to the focus position. When the SPPM is placed far enough out of focus, the beam is larger than the SPPM and partially reflects off the surrounding substrate. In the NF, the two parts of the beam interfere to form a characteristic spiral pattern, indicating the presence of OAM [25]. As the SPPM is translated closer to focus, it reflects the beam completely, forming a donut-shaped pattern.

Next, we tested the performance of the targets at laser intensities above the plasma formation threshold, using a multi-TW Ti:Sapphire laser system. In these experiments, we used a 1.5 cm diameter aperture to maintain a nearly-uniform flat-top beam, with 5 mJ energy per pulse and 25 fs duration. A low-power measurement of the collimated beam profile is shown in figure 4(a). The beam was focused by a 16.3 cm focal length off-axis parabolic mirror to form a  $20 \mu\text{m}$  diameter Airy disk intensity pattern on the target, shown in figure 4(b). The SPPM targets were irradiated at peak intensity of  $10^{17} \text{ W cm}^{-2}$ . At this intensity, we expect the plasma expansion to be a few times  $\lambda/100$  [26], thus having minimal effect on the reflected beam properties. The laser pulses reflected from the targets were collected by a 15 cm focal length lens and split to collimated- and focused-beam imaging systems. The collimated-beam imaging system consisted of a white screen imaged by a CCD camera. The focal-plane images were acquired directly by a CCD detector, placed 225 cm beyond the collecting lens, providing  $15 \times$  magnification.

Before each shot, the target manipulator was translated to expose a fresh SPPM target. The targets were aligned to beam center with a  $1 \mu\text{m}$  resolution. The alignment at each shot was performed with the laser operated at its lowest intensity, to produce annular beam patterns in the beam diagnostics. During the first shots, a systematic shift of the

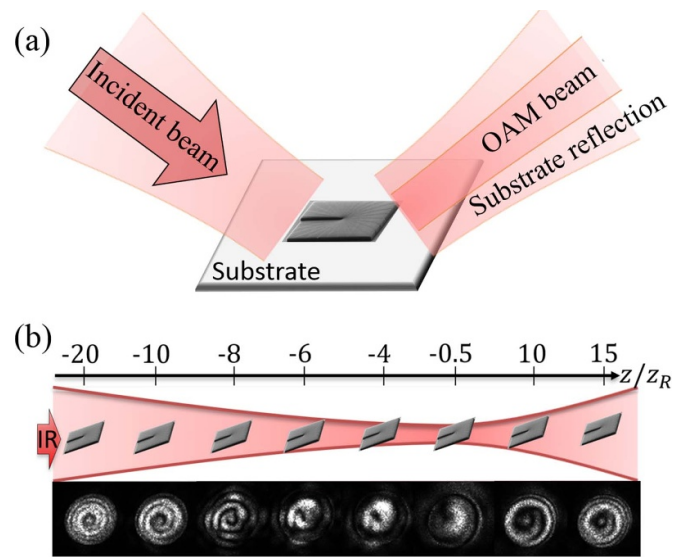


**Figure 3.** (a) Illustration of co-linear interference in CW mode. A low power CW beam reflect off the Au-coated front surface of an  $l = 1$  SPPM element at  $55^\circ$  AOI. Since the beam is larger then the SPPM when out-of-focus, some light is also reflected from the surrounding substrate. Away from the target plane, the two parts of the beam interfere co-linearly. (b) CW interference patterns, measured for different positions of the SPPM target. The cartoon illustrates the position of the SPPM with respect to the incident laser beam. Here,  $z_R$  is the Rayleigh length of the incident beam. The interference patterns clearly justify the topological charge  $l = 1$  (see [25]).

laser pointing was recognized, by comparing the pre-shot and on-shot beam patterns. In the following shots, the targets were positioned to pre-compensate for the expected pointing shift.

At full power shots, shown in figures 4(c) and (d), the collimated and focused profiles clearly show that the annular pattern characterizing an OAM beam is preserved when reflecting from the plasma surface. The asymmetry of the focused beam in figure 4(d) is a result of small misalignment between the incident beam, and the SPPM. Following irradiation, the SPPM and its vicinity are completely ablated, as shown in figures 4(g) and (h). To validate these results, we calculated

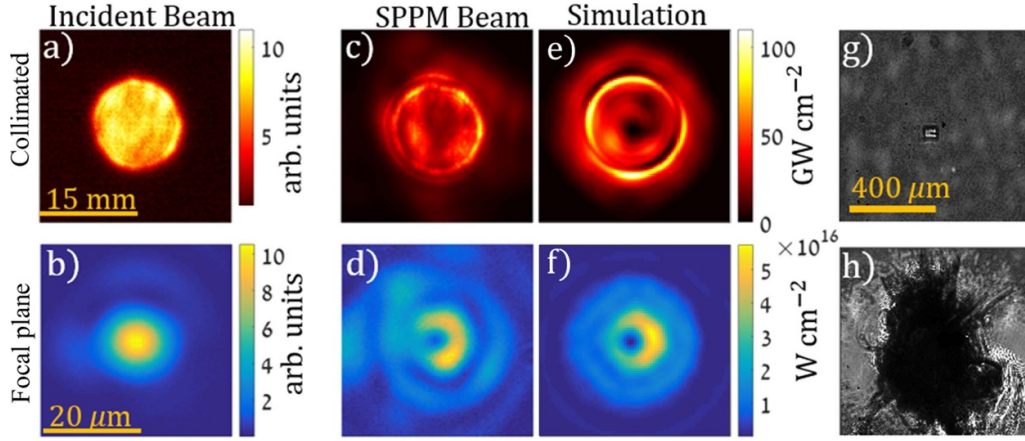


**Figure 4.** Beam profiles of a femtosecond laser reflected off an  $l = 1$  SPPM. (a) and (b) Collimated and focused images of the incident beam. (c) and (d) Collimated and focused beam profiles after reflection off SPPM at high-intensity  $I = 10^{17} \text{ W cm}^{-2}$ . (e) and (f) Simulation of the expected collimated and focused intensity distributions after reflection off the SPPM. Images of an SPPM (g) before and (f) after a shot.

the expected collimated and focused profiles by assigning a phase term to the incident laser at the focus:

$$E_{\text{OAM}}(x, y) = E_L(x, y) \exp(-i\phi_{\text{SPPM}}(x, y)), \quad (4)$$

with  $E_L(x, y)$  being in the form of an ideal Airy disk pattern and  $\phi_{\text{SPPM}}(x, y)$  is the phase induced by the target, given by:

$$\begin{aligned} \phi_{\text{SPPM}}(x, y) = & \cos \theta_{\text{AOI}} z \left( \frac{x}{\cos \theta_{\text{AOI}}}, y \right) \\ & \times \Theta \left( \frac{D_x}{2} - \frac{|x|}{\cos \theta_{\text{AOI}}} \right) \Theta \left( \frac{D_y}{2} - |y| \right). \end{aligned} \quad (5)$$

Here,  $z(x, y)$  is given by equation (3), and the Heaviside functions  $\Theta(x)$  define the SPPM boundaries, with  $D_x$ ,  $D_y$  being the length and width of the target. To simplify the calculation, we approximated the phase-front curvature in equation (3) to an ideal sphere by setting  $x_0 = y_0 = 1$ ,  $R_{xy} = 0$  and  $R_y = R_x \cos^2 \theta_{\text{AOI}} = R$ . For  $\theta_{\text{AOI}} = 55^\circ$ , the average ROC is  $R = -550 \pm 123 \mu\text{m}$ .

The curved surface shifts the reflected beam waist to  $z_0 = (2/R + R/2z_R^2)^{-1}$  [27]. Here  $z_R = \frac{1}{2}kw_0^2$  is the Rayleigh length of the incident beam, and  $w_0$  is its Rayleigh disk radius. The focused beam profile is calculated by propagating the beam from the focal plane to the new waist position in the Fresnel approximation. The collimated profile is calculated in the Fraunhofer approximation at one focal distance away. The calculated collimated and focused profiles are shown in figures 4(e) and (f). These results capture the main spatial features of the measured beam, including the energy spread around the original beam perimeter in the collimated beam, and the secondary ring structure in the focused beam. These features indicate that the generated beam is not a pure LG beam, which is a result of the finite size of the SPPM as well as the original beam quality. The asymmetry of the focused beam is captured by introduction of  $\approx 0.5 \mu\text{m}$  lateral misalignment between the laser beam and the SPPM, which is within our alignment accuracy.

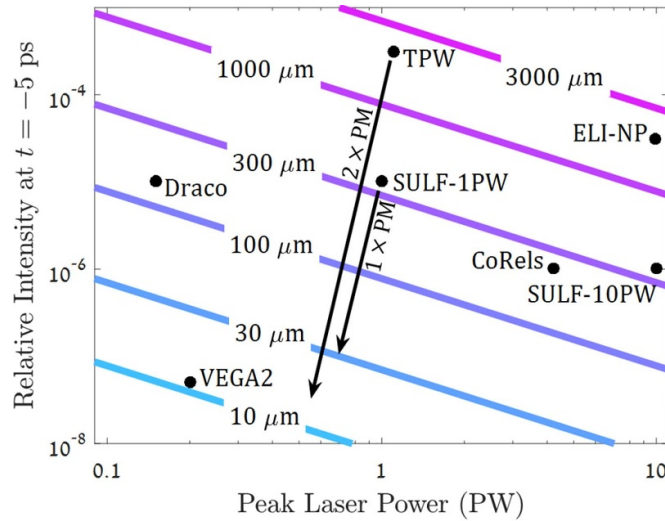
#### 4. Discussion

The main prospect for SPPMs is with PW laser systems, where dielectric SPM optics become highly expensive. Scaling the above demonstration from TW to PW lasers would require additional considerations. First, pre-expansion of the target, which may alter its spatial properties, must be mitigated by ensuring that the laser intensity on-target does not exceed the ablation threshold up to a few ps before the peak of the pulse. For any realistic laser system with peak power  $P_0$ , the temporal contrast  $\epsilon$  is defined as the ratio of  $P_0$  to any preceding light, e.g. pre-pulses, up to some time  $t_0$  prior to its peak,  $P(t) < \epsilon P_0$  for any  $t < -t_0$ . To prevent pre-expansion, the focused intensity of any preceding light must be limited to below the target's ablation threshold  $I_{\text{ab}}$ . We note that in the ultra-short, ultra-intense laser parameters considered here, the damage threshold is related to the on-target laser intensity ( $\text{W cm}^{-2}$ ), rather than to the laser fluence ( $\text{J cm}^{-2}$ ), which is the typical figure of merit in longer pulse durations. This constrains the minimum lateral dimension of the laser spot, and correspondingly the SPPM dimension to:

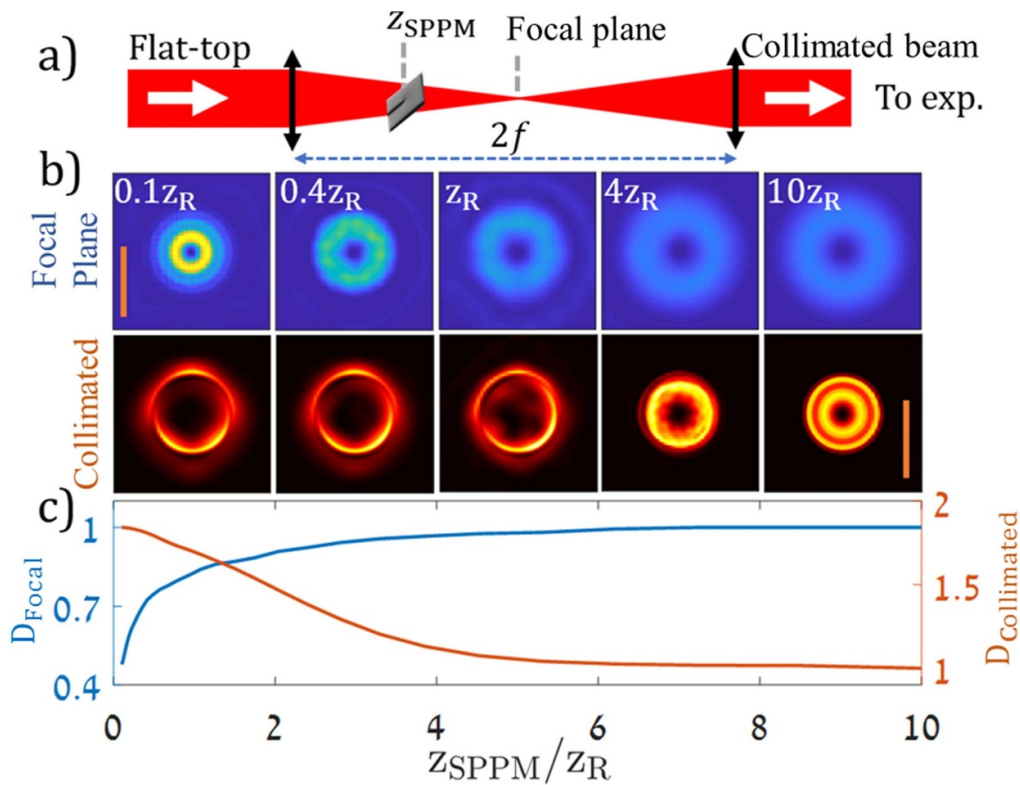
$$w_{\text{SPPM}} > 2\sqrt{\frac{\epsilon P_0}{\pi I_{\text{ab}}}}. \quad (6)$$

Figure 5 presents the minimal SPPM dimension predicted by equation (6), as a function of the peak laser power and the laser intensity contrast at  $t_0 = 5 \text{ ps}$ . The laser pulse specifications of several contemporary ultra-high-power laser systems are also indicated on the figure. Plasma pre-expansion during this 5 ps interval would amount to a plasma scale length shorter than  $0.2\lambda$  [28], assuming an ablation threshold of  $\sim 10^{13} \text{ W cm}^{-2}$  [29–31]. The minimal SPPM dimension varies from tens of microns for very-high-contrast laser systems to a few millimeters in laser systems having moderate contrast.

Although fabrication of SPPMs using 3D-DLW is feasible in this entire range, a large target size involves prolonged manufacturing, which could amount to several hours per target. A



**Figure 5.** Contour plot of the minimal target size as a function of the laser peak power and contrast at  $t = -5$  ps. The pulse specifications of several ultra-high-power laser systems are also shown.



**Figure 6.** (a) Schematic  $2f$  SPPM beam shaping. In a realistic setup the SPPM and focusing optics are all reflective. In (b) calculated focused (top panel) and collimated (bottom panel) profiles following a reflection off an SPPM that is placed at different distances from the focal point. The lateral scales of the unperturbed flat-top beam diameter in the focal plane and in the collimated beam are indicated by orange bars. (c) Calculated beam diameters in the focal plane (blue) and collimated beam (orange) as a function of SPPM position. Beam diameters are normalized to their value in the limit of  $z_{\text{SPPM}} \gg z_R$ .

more feasible solution would be to use one or two flat PMs before the SPPM to improve the temporal contrast. The effect of this method on the required SPPM dimensions is illustrated in figure 5 by arrows for two laser systems. In this calculation, each PM was assumed to have 75% reflectivity and to improve the temporal contrast by two orders of magnitude.

The minimal spot sizes presented in figure 5 would be impractical to achieve in most PW-class systems if the SPPM is positioned at the focal plane. Thus, the SPPM would be placed out of focus. Figure 6(a) illustrates an SPPM beam-line. Varying the SPPM position relative to the focal plane can affect the shaped beam profile, as suggested by the focused

and collimated simulations of the reflected beam, shown in figure 6(b) when the SPPM is placed at different distances  $z_{\text{SPPM}}$  from the focus. Here, the dimensions of the target were kept to 150% of the beam diameter at each SPPM position. We also assume ideal fabrication to neglect the overall curvature of the target. The evolution of the beam diameter with the SPPM position is shown in figure 6(c). In the focal plane, the beam size was quantified according to the radius of maximum intensity. The collimated beam diameter was characterized using the ISO beam width definition [32], which offers a more robust treatment of the irregular intensity distributions at small values of  $z_{\text{SPPM}}$ . The focused beam radius is highly sensitive to the SPPM position near the focus, and it displays an asymptotic behavior at a large distance. The collimated beam presents irregular intensity spread, including hot spots and a wide energy scatter at small values of  $z_{\text{SPPM}}$  which slowly moderates at a few Rayleigh lengths from the waist. The irregularities originate from the finite size of the SPPM, relative to the wide energy spread of the Airy pattern. At  $z_{\text{SPPM}} \gg z_{\text{R}}$ , the collimated beam diameter becomes similar to the original aperture. This analysis indicates that placing the SPPM at a few Rayleigh lengths away from focus would yield a stable predictable OAM beam, and will not require changing the downstream optics of the laser line. Another practical benefit for out-of-focus SPPM position is the lower sensitivity to the laser's pointing stability away from the focal plane.

## 5. Conclusion

In this paper we demonstrated the generation of high intensity OAM beams using 3D-DLW fabricated SPPMs. This method provides an economic and scalable solution for ultra-high-intensity laser systems, and it is relatively straightforward to implement in PW-level beam lines. For the current proof-of-concept, a single SPPM design was demonstrated, at specific topological number, spot size and AOI. However, owing to the versatility of the 3D-DLW technique, the SPPM method can be easily extended to higher OAM modes as well as Hermite-Gauss and Bessel beams. These extensions will be the subject of future work. In a wider context, the demonstration of DLW of structured PM targets paves the way for realization of relativistic plasma optics, such as micro-tube lenses [33] and relativistic high-order harmonics focusing [34].

## Data availability statement

All data that support the findings of this study are included within the article (and any supplementary files).

## Acknowledgments

We acknowledge aid in target fabrication from the Hebrew University Center for Nanoscience and Nanotechnology. We acknowledge the support by the Pazy Foundation, Grant #27707241, and by the Zuckerman STEM Leadership Program.

## ORCID iDs

Elkana Porat  <https://orcid.org/0000-0003-4004-2945>

Isahy Pomerantz  <https://orcid.org/0000-0001-9824-887X>

## References

- [1] Allen L, Beijersbergen M W, Spreeuw R J C and Woerdman J P 1992 Orbital angular momentum of light and the transformation of Laguerre–Gaussian laser modes *Phys. Rev. A* **45** 8185–9
- [2] Padgett M and Bowman R 2011 Tweezers with a twist *Nat. Photon.* **5** 343–8
- [3] Hell S W and Wichmann J 1994 Breaking the diffraction resolution limit by stimulated emission: stimulated-emission-depletion fluorescence microscopy *Opt. Lett.* **19** 780
- [4] Wang J et al 2012 Terabit free-space data transmission employing orbital angular momentum multiplexing *Nat. Photon.* **6** 488–96
- [5] Molina-Terriza G, Torres J P and Torner L 2007 Twisted photons *Nat. Phys.* **3** 305–10
- [6] Wang W P, Jiang C, Shen B F, Yuan F, Gan Z M, Zhang H, Zhai S H and Xu Z Z 2019 New optical manipulation of relativistic vortex cutter *Phys. Rev. Lett.* **122** 024801
- [7] Wang W, Shen B, Zhang X, Zhang L, Shi Y and Zhizhan X 2015 Hollow screw-like drill in plasma using an intense Laguerre–Gaussian laser *Sci. Rep.* **5** 8274
- [8] Vieira J, Mendonça J T and Quéré F 2018 Optical control of the topology of laser-plasma accelerators *Phys. Rev. Lett.* **121** 054801
- [9] Li-Xiang H, Tong-Pu Y, Sheng Z-M, Vieira J, Zou D-B, Yin Y, McKenna P and Shao F-Q 2018 Attosecond electron bunches from a nanofiber driven by Laguerre–Gaussian laser pulses *Sci. Rep.* **8** 7282
- [10] Zhang X, Shen B, Shi Y, Wang X, Zhang L, Wang W, Jiancai X, Longqiong Y and Zhizhan X 2015 Generation of intense high-order vortex harmonics *Phys. Rev. Lett.* **114** 173901
- [11] Vieira J, Trines R M G M, Alves E P, Fonseca R A, Mendonça J T, Bingham R, Norreys P and Silva L O 2016 High orbital angular momentum harmonic generation *Phys. Rev. Lett.* **117** 265001
- [12] Zhu X L, Chen M, Yu T P, Weng S M, Hu Li X, McKenna P and Sheng Z M 2018 Bright attosecond  $\gamma$ -ray pulses from nonlinear Compton scattering with laser-illuminated compound targets *Appl. Phys. Lett.* **112** 174102
- [13] Denoed A, Chopineau L, Leblanc A and Quéré F 2017 Interaction of ultraintense laser vortices with plasma mirrors *Phys. Rev. Lett.* **118** 033902
- [14] Brabetz C, Busold S, Cowan T, Deppert O, Jahn D, Kester O, Roth M, Schumacher D and Bagnoud V 2015 Laser-driven ion acceleration with hollow laser beams *Phys. Plasmas* **22** 013105
- [15] Ghai D P 2011 Generation of optical vortices with an adaptive helical mirror *Appl. Opt.* **50** 1374–81
- [16] Longman A et al 2020 Off-axis spiral phase mirrors for generating high-intensity optical vortices *Opt. Lett.* **45** 2187
- [17] Von der Linde D, Sokolowski-Tinten K and Bialkowski J 1997 Laser–solid interaction in the femtosecond time regime *Appl. Surf. Sci.* **109** 1–10
- [18] Leblanc A, Denoed A, Chopineau L, Mennerat G, Martin P and Quéré F 2017 Plasma holograms for ultrahigh-intensity optics *Nat. Phys.* **13** 440–3
- [19] Kenan Q, Jia Q and Fisch N J 2017 Plasma q-plate for generation and manipulation of intense optical vortices *Phys. Rev. E* **96** 053207

- [20] Vieira J, Trines R M G M, Alves E P, Fonseca R A, Mendonça J T, Bingham R, Norreys P and Silva L O 2016 Amplification and generation of ultra-intense twisted laser pulses via stimulated Raman scattering *Nat. Commun.* **7** 10371
- [21] Shi Y, Shen B, Zhang L, Zhang X, Wang W and Zhizhan X 2014 Light fan driven by a relativistic laser pulse *Phys. Rev. Lett.* **112** 235001
- [22] Brasselet E, Malinauskas M, Žukauskas A and Juodkazis S 2010 Photopolymerized microscopic vortex beam generators: precise delivery of optical orbital angular momentum *Appl. Phys. Lett.* **97** 211108
- [23] Longman A and Fedosejevs R 2017 Mode conversion efficiency to Laguerre–Gaussian OAM modes using spiral phase optics *Opt. Express* **25** 17382
- [24] Dromey B et al 2009 Diffraction-limited performance and focusing of high harmonics from relativistic plasmas *Nat. Phys.* **5** 146–52
- [25] Vickers J, Burch M, Vyas R and Singh S 2008 Phase and interference properties of optical vortex beams *J. Opt. Soc. Am. A* **25** 823
- [26] Porat E, Yehuda H, Cohen I, Levanon A and Pomerantz I 2021 Diffraction-limited coherent wake emission *Phys. Rev. Res.* **3** L032059
- [27] Self S A 1983 Focusing of spherical Gaussian beams *Appl. Opt.* **22** 658
- [28] Kahaly S et al 2013 Direct observation of density-gradient effects in harmonic generation from plasma mirrors *Phys. Rev. Lett.* **110** 175001
- [29] Fernández-Pradas J M, Florian C, Caballero-Lucas F, Morenza J L and Serra P 2013 Femtosecond laser ablation of polymethyl-methacrylate with high focusing control *Appl. Surf. Sci.* **278** 185–9
- [30] Baudach S, Bonse J and Kautek W 1999 Ablation experiments on polyimide with femtosecond laser pulses *Appl. Phys. A* **69** S395–8
- [31] Koch J, Fadeeva E, Engelbrecht M, Ruffert C, Gatzel H H, Ostendorf A and Chichkov B N 2006 Maskless nonlinear lithography with femtosecond laser pulses *Appl. Phys. A* **82** 23–26
- [32] ISO 11145 2018 *optics and photonics-lasers and laser-related equipment-vocabulary & symbols* (<https://doi.org/10.31030/2867155>)
- [33] Ji L L, Snyder J, Pukhov A, Freeman R R and Akli K U 2016 Towards manipulating relativistic laser pulses with micro-tube plasma lenses *Sci. Rep.* **6** 23256
- [34] Vincenti H 2019 Achieving extreme light intensities using optically curved relativistic plasma mirrors *Phys. Rev. Lett.* **123** 105001